

7-2016

Photodissociation Dynamics of OCS near 214 nm Using Ion Imaging

Wei Wei

Texas A & M University - College Station

Colin J. Wallace

Texas A & M University - College Station

George McBane

Grand Valley State University, mcbaneg@gvsu.edu

Simon W. North

Texas A & M University - College Station

Follow this and additional works at: https://scholarworks.gvsu.edu/chm_articles

 Part of the [Chemistry Commons](#)

ScholarWorks Citation

Wei, Wei; Wallace, Colin J.; McBane, George; and North, Simon W., "Photodissociation Dynamics of OCS near 214 nm Using Ion Imaging" (2016). *Peer Reviewed Articles*. 30.

https://scholarworks.gvsu.edu/chm_articles/30

This Article is brought to you for free and open access by the Chemistry Department at ScholarWorks@GVSU. It has been accepted for inclusion in Peer Reviewed Articles by an authorized administrator of ScholarWorks@GVSU. For more information, please contact scholarworks@gvsu.edu.

Photodissociation Dynamics of OCS Near 214 nm Using Ion Imaging

Wei Wei^a, Colin J. Wallace^a, George C. McBane^b, and Simon W. North^{a,*}

^aDepartment of Chemistry, Texas A&M University, College Station, Texas 77842

^bDepartment of Chemistry, Grand Valley State University, Allendale, Michigan 49401

Abstract: The OCS photodissociation dynamics of the dominant S(¹D₂) channel near 214 nm have been studied using velocity map ion imaging. We report a CO vibrational branching ratio of 0.79:0.21 for v=0:v=1, indicating substantially higher vibrational excitation than that observed at slightly longer wavelengths. The CO rotational distribution is bimodal for both v=0 and v=1, although the bimodality is less pronounced than at longer wavelengths. Vector correlations, including rotational alignment, indicate that absorption to both the 2¹A' (A) and 1¹A'' (B) states is important in the lower-*j* part of the rotational distribution, while only 2¹A' state absorption contributes to the upper part; this conclusion is consistent with work at longer wavelengths. Classical trajectory calculations including surface hopping reproduce the measured CO rotational distributions and their dependence on wavelength well, though they underestimate the v=1 population. The calculations indicate that the higher-*j* peak in the rotational distribution arises from molecules that begin on the 2¹A' state but make nonadiabatic



This manuscript was accepted by J. Chem. Phys. Click [here](#) to see the version of record.

transitions to the $1^1A'$ (X) state during the dissociation, while the lower- j peak arises from direct photodissociation on either the $2^1A'$ or the $1^1A''$ states, as found in previous work.

Submitted to: The Journal of Chemical Physics June 10, 2016

2 Tables, 8 Figures

proofs to: Simon W. North

Department of Chemistry

Texas A&M University

P.O. Box 30012

College Station, TX 77842

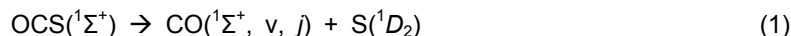
Fax: 979-845-2971

e-mail: swnorth@tamu.edu

I. Introduction

Carbonyl sulfide (OCS), the most abundant sulfur containing compound in the atmosphere,¹ is emitted into the troposphere by both biogenic and anthropogenic sources. The burning of biomass and natural gas and the oxidation of dimethyl sulfide and carbon disulfide account for the majority of OCS production.^{2,3} OCS is relatively inert with a global lifetime of 3.7 years in the troposphere, resulting in partial transport to the stratosphere where the lifetime is 63 ± 15 years,^{4,5} with photolysis as the major loss pathway. The UV absorption spectrum of OCS shows a broad Gaussian-like peak near 223 nm with weak vibrational structure.^{6,7,8,9,10} The lowest energy levels in linear OCS are the ground $1\Sigma^+$ state and the excited $1\Sigma^-$ and 1Δ states. Transitions from the ground state to $1\Sigma^-$ and 1Δ states are forbidden by symmetry for linear OCS. Upon bending, the $1\Sigma^+$ state becomes $1^1A'$ (called X by Schmidt *et al.*,¹¹ whose naming we will follow). The $1\Sigma^-$ state becomes $1^1A''$ (B) on bending, and the 1Δ state splits into a Renner-Teller pair $2^1A'$ (A) and $2^1A''$ (C). The A and B states have shallow wells at bent geometries, and dissociate directly. The C state and the very similar $2^3A''$ (c) state have deep wells at linear or nearly linear geometries and are quasibound. Transitions in bent OCS from the ground state to the A and B states contribute the smooth main part of its first absorption band, and Schmidt *et al.* concluded that transitions to C and c produce the superimposed vibrational structure.¹¹

There are two sulfur product channels in OCS photodissociation,



with the singlet channel (1) dominant at all wavelengths studied. At 222 nm, approximately 94% proceeds to the singlet channel.¹² We examine the singlet pathway in the present work.

The CO bond length is only 3% shorter in CO than in OCS, and the dissociation produces a cold CO vibrational state distribution. Sivakumar et al. observed no vibrationally excited CO following photolysis at any of 222, 235, and 248 nm and gave upper limits of 2% $v=1$ at 222 nm and 6% at 235 nm.¹³ Sato et al. also detected no $v>0$ CO.¹⁴ Rijs et al. did detect a small amount of $v=1$ CO at 230 nm, but did not give a quantitative estimate of the branching ratio.¹⁵ Lee et al. saw hints of vibrationally excited, possibly including $v=4$, CO following 193 nm dissociation.¹⁶

Strong bending forces on the A and B state surfaces during the dissociation result in rotationally excited CO fragments. Sivakumar et al. were the first to observe the highly excited and bimodal rotational state distribution at 222 nm, with a main peak at $j=56$ and a subsidiary maximum at $j=67$.¹³ Subsequent work by other groups showed that the bimodal character persists for photolysis wavelengths between 248 and 193 nm.^{14,15,17,18} As the excitation energy increases, the higher- j peak becomes more pronounced, both components of the rotational distribution shift to higher j , and the spacing between the two components diminishes. By 217 nm the two rotational distributions partially coalesce,¹⁴ and at 193 nm the

high- J peak is the largest.¹⁶ At 288 nm in the far red wing of the absorption band, little excess energy remains for rotational excitation.¹⁹

Product angular distributions $I(\theta)$ have been reported at several dissociation wavelengths.^{12,13,14,17,18,19,20,21,22} These are characterized by the spatial anisotropy parameter β according to $I(\theta) \propto 1 + \beta P_2(\cos \theta)$ where P_2 is the second Legendre polynomial and θ is the angle between the outgoing fragment velocity and the polarization vector of the photodissociating light. For a linear molecule in the axial recoil limit, β is +2 for a purely parallel transition ($\Delta\Omega=0$) and -1 for a purely perpendicular transition ($\Delta\Omega=\pm 1$).^{23,24} For dissociation of bent but rotationless OCS, absorption to an A'' state will necessarily produce $\beta = -1$, while absorption to an A' state may produce any value of β between 2 and -1 depending on the orientation of the transition dipole in the molecular plane and the extent of nonaxial recoil. Most experiments indicate that β generally increases with CO rotational state, from relatively small positive values at the lowest populated j state to near the limiting value of 2 in the upper part of the rotational distribution. At 288 nm the slightly lower-energy B state dominates the absorption and $\beta \approx -0.7$.¹⁹

Sivakumar et al. also measured the CO rotational alignment, the distribution of CO angular momentum vectors \mathbf{j} with respect to the polarization vector $\boldsymbol{\mu}$ of the photolysis light.¹³

The $\boldsymbol{\mu}$ - \mathbf{j} correlation is the experimental observable best suited to distinguish between products formed via A' or A'' state excitation. Conservation of angular momentum constrains \mathbf{v} to be perpendicular to \mathbf{j} for photodissociation of a $j=0$ triatomic molecule. Since $\boldsymbol{\mu}$ lies in the OCS plane for the A' state excitation, $\boldsymbol{\mu}$ and \mathbf{j} must be perpendicular, while for the A'' state

excitation μ and j must be parallel. Therefore, determination of the μ - j correlation can provide quantitative information regarding the relative contributions of the two product channels. Sivakumar *et al.* made the only previous measurements of this quantity for OCS, at 222 nm, and used them to estimate the fractional contributions of different electronic states as a function of product rotational state.¹³ In this paper we report new measurements of CO rotational alignment for dissociation near 214 nm.

The current understanding of OCS photodissociation dynamics in the first absorption band indicates that absorption to the A and B states play roughly comparable roles in the lower part of the rotational distribution,^{13,18,25} while the upper part is contributed by absorption to the A state followed by nonadiabatic transitions to the ground state. Nonaxial recoil is important for both A and B state dissociations. The transition moment for the A-state absorption, which must lie in the triatomic plane, is displaced from the OCS axis by 30-40 degrees, compensating for nonaxial recoil and yielding β parameters near 2 despite its presence.^{22,25} Absorption to the B state necessarily produces $\beta=-1$ for nonrotating OCS. The variation in β across the lower part of the rotational distribution reflects the relative contributions of the A and B states and their slightly different rotational distributions. The crucial transition dipole functions are relatively difficult to calculate accurately with electronic structure methods,¹¹ and the relative contribution of A and B states has therefore been the slowest part of the dynamical picture to come to consensus.

In this work we report experimental product state distributions, angular distributions, and rotational alignments for OCS photodissociation dynamics near 214 nm, extending previous

similar measurements to shorter wavelength. The rotational distributions of the CO product for both $v=0$ and $v=1$ measured using 2+1 REMPI are bimodal but only partially resolved, reflecting the merging of the two rotational components that are resolved at longer wavelength. $S(^1D_2)$ images were collected to confirm the CO rotational distributions. The spatial anisotropy distribution obtained from the $S(^1D_2)$ image indicates that β increases in value from low j to high j , consistent with results at longer wavelength. CO fragment vector correlations including rotational alignments confirm that both $2^1A'$ and $1^1A''$ absorptions contribute to the low j component while the $2^1A'$ state is the main contributor to the high j component. Most of the experimental results agree satisfactorily with corresponding surface-hopping calculations.

II. Experimental

The molecular beam/velocity-map ion-imaging apparatus has been described in detail elsewhere,²⁶ although the detector region has been modified and the length of the flight tube increased to 76 cm. The turbopumped vacuum system consists of source, main, and detector regions, arranged collinearly. A free jet expansion is produced by a General Valve series 9 pulsed valve in the source chamber whose pressure is typically 9×10^{-5} torr. An electroformed skimmer collimates the molecular beam and separates the source and main (interaction) regions. Pressures in the main region are typically 2×10^{-6} torr with minimal change when the pulsed valve is operating. Two windows allow counterpropagating laser beams to intersect the molecular beam at 90° . Four einzel lenses accelerate photoions toward the detector and provide velocity mapping. The detector region is separated from the main chamber by a gate valve and is kept at pressures near 1×10^{-7} torr during operation. The detector, which faces the

beam source, consists of a pair of chevron microchannel plates (MCP) with a P51 phosphor screen. A Hamamatsu R928 photomultiplier tube or an IDS uEye gated CCD camera are used to record the signal from the phosphor screen. The source gas was made by flowing 1 atm of helium through a bubbler containing OCS at 196 K, yielding ~25% OCS in the molecular beam. Measurements using a 5% mixture of CO and helium gas yielded a principal rotational temperature of about 8 K with a small high- j tail.

Linearly polarized 214 nm light was generated by the third harmonic of a Spectra Physics Lab-150-10 Nd:YAG laser (355 nm) which pumped a Lambda Physik Scanmate dye laser to generate 430 nm. The dye laser output was frequency doubled using a type I BBO crystal to generate wavelengths corresponding to the $2 + 1$ REMPI transitions of CO through the E-X (0,0) band (213-216 nm).^{27,28} The laser beam was focused into the interaction region using a 25 cm focal length lens. Experimental images of the CO fragment employed only one color. Experimental images of the sulfur atom fragment employed a second counterpropagating dye laser for $2+1$ REMPI detection. The sulfur probe beam was generated by the second harmonic of a Spectra Physics Lab-150-10 Nd:YAG (532 nm) which pumped a PDL-1 dye laser (Rhodamine 610) with wavelengths ranging from 583 to 595 nm. The output was frequency doubled for the $2+1$ REMPI transition of S(1D_2) at 290.18 nm via the 3P_1 intermediate state^{29,30} and focused into the interaction region using a 30 cm focal length lens. The polarization of either laser could be set to be parallel to the image plane (later noted as V) or perpendicular to the image plane (H). The focus of the 214 nm pump beam was detuned when collecting the sulfur images. Typical energies for the 214 nm and 290 nm pulses were 500 μ J/pulse and 900

μJ / pulse respectively. The pump-probe delay time used for the two-color experiment was approximately 25 ns. The crushed sulfur images were obtained with both the dissociation and probe laser beams vertically polarized, yielding cylindrical symmetry in the ion cloud, in order to permit polar onion peeling to reconstruct the full 3D images resulting in speed distributions.³¹ The MCP time gating was 100 ns for crushed images. The DC sliced images were treated using the finite slice algorithm described by Komissarov *et al.* to obtain speed distributions.³² The resulting speed distribution was treated with a polynomial fit to subtract the background signal. The MCP time gating was 40 ns for sliced images resulting in a finite slice of ~20%.

III. Calculations

The classical calculations were carried out as described in references 25 and 33, using the empirically modified adiabatic surfaces for the A and B states described in reference 25. Schmidt and Olsen recently found, using a two-dimensional study with accurate electron correlation methods, that the empirical modification to those surfaces was at least qualitatively reasonable.³⁴ As in reference 25, the total energy was reduced by 0.1 eV in order to compensate for unphysical distribution of the CO zero point energy into product rotation. To model photodissociation at 214.5 nm from the ground state of OCS whose zero point energy is 0.245 eV, initial conditions were therefore selected to have total energies within 0.01 eV of 5.925 eV. Composite properties arising from trajectories on both A/X and B states were computed as described in Section V.A of reference 25, using a cross section ratio $\sigma_A/\sigma_B=2.0$ for 214.5 nm.³⁵

Nonadiabatic coupling between the A and X surfaces was modeled with the trajectory surface hopping method of Tully,^{36,37} using only the γ component of the nonadiabatic coupling vector. Total energy was conserved at hops by distributing the change in potential energy “democratically” among the three Jacobi momenta, because this approach was found to be preferable for computation of angular distributions.³³

IV. Results and Discussion

A. Product Internal State Distributions

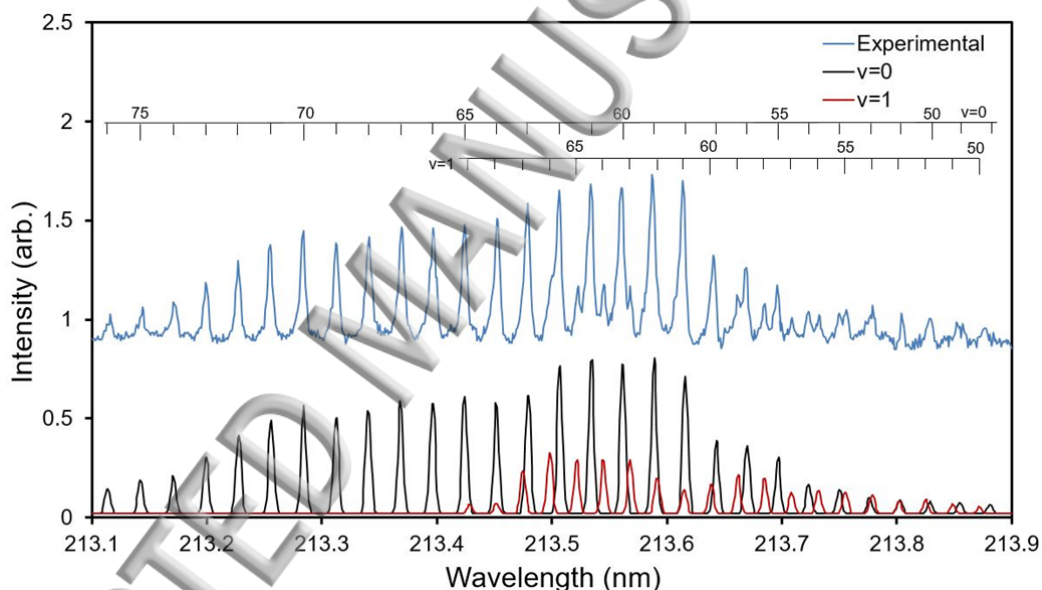


Figure 1. $2 + 1$ REMPI scan of the CO S-branch from the one color photodissociation of OCS. The experimental data (upper trace) shows the clearly resolved $v=0$ and $v=1$ components. Simulated spectra for the $v=0$ (black) and $v=1$ (red) contributions are shown below.

A representative experimental $2+1$ E-X REMPI scan of the CO fragment arising from OCS photodissociation near 213.5 nm is shown in Figure 1. Two-color imaging experiments probing the $S(1D_2)$ fragment indicated that the small change in dissociation wavelength, over a region similar in range to that of Figure 1, did not yield measurably different CO rotational populations.

We therefore believe that the one-color measurements can be used to determine the CO rotational distribution over the narrow range of wavelengths employed. In the CO REMPI spectrum there are two clear sets of peaks corresponding to transitions associated with the (0,0) and (1,1) bands. The simulated (0,0) and (1,1) bands are shown as black and red respectively in the lower panel of Figure 1. The observed rotational states range from $j=48-76$ for the (0,0) band and $j=50-69$ for the (1,1) band. Quantitative comparison of the simulated REMPI spectrum with the experimental data required optimization of spectroscopic constants in order to obtain reasonable fits for both transitions. The spectroscopic constants were determined by fitting the peak positions to

$$E_{hv} = [T_{vv} + B'_v j'(j' + 1) - D'_v j'^2(j' + 1)^2] - [B''_v j''(j'' + 1) - D''_v j''^2(j'' + 1)^2]. \quad (3)$$

The initial B_v'' , D_v'' , B_v' , D_v' , T_{00} for $v=0$ and $v=1$ were taken from Baker *et al.*³⁸ T_{11} was calculated by taking the difference of T_{10} from Baker *et al.*³⁸ and v_0 from Plyler *et al.*³⁹ Using these values as a starting point, all of the parameters were optimized resulting in effective spectral constants for the X and E states. The final values used in the spectral simulations are shown in Table I.

Table I. The spectroscopic constants used to both fit the CO 2+1 REMPI spectra and simulate the sulfur speed distribution. All values reported are in cm^{-1} .

* T_{11} was calculated by taking the difference between T_{10} (95081.9 cm^{-1}) from Baker *et al.*³⁸ and v_0 (2143.2 cm^{-1}) from Plyler *et al.*³⁹

	B_v''	D_v''	B_v'	D_v'	T_{vv}
$v=0$	1.8889	5.477×10^{-6}	1.9312	5.908×10^{-6}	92929.95^{38}
$v=1$	1.8924	6.1244×10^{-6}	1.9261	7.1526×10^{-6}	92939.7^*

Simulations of the REMPI of the (0,0) and (1,1) bands are shown with solid black and red lines, respectively. Several of the peaks associated with the individual vibronic bands overlap in the spectrum, making a determination of relative intensities difficult. In order to determine the relative populations of the overlapping peaks, we collected CO ion images at wavelengths corresponding to the overlapping states: at 213.458 nm ($j=64$ $v=0$ and $j=68$ $v=1$), 213.478 nm ($j=63$ $v=0$ and $j=67$ $v=1$), 213.615 nm ($j=58$ $v=0$ and $j=61$ $v=1$) and 213.641 nm ($j=57$ $v=0$ and $j=60$ $v=1$). The relative intensity from each overlapped feature is obtained by integrating the intensity of each contribution. The non-overlapped $v=0$ and $v=1$ transition peaks were fit directly. The overall $v=1$ population is estimated based on the peak area of all the peaks from $v=1$ transitions over the sum of the peak areas from both the $v=1$ and $v=0$ transitions,

$$P(v = 1) = \frac{\sum_{j=0,v=1} I(j)}{\sum_{j=0,v=0} I(j) + \sum_{j=0,v=1} I(j)} \quad (4)$$

The simulated spectrum is in good agreement with the experimental REMPI spectrum. The consistent trend of transitions rules out possibilities of isolated perturbations. The

Franck-Condon factors of (0,0) and (1,1) bands, computed using Morse potentials for the E and X states,⁴⁰ differ by less than 4%. However, a smooth competition between predissociation and ionization can still not be eliminated. A difference in ionization probability between $v=0$ and $v=1$ CO could affect the fraction of $v=1$ determined via Equation 4. No attempts are made to correct for these issues.

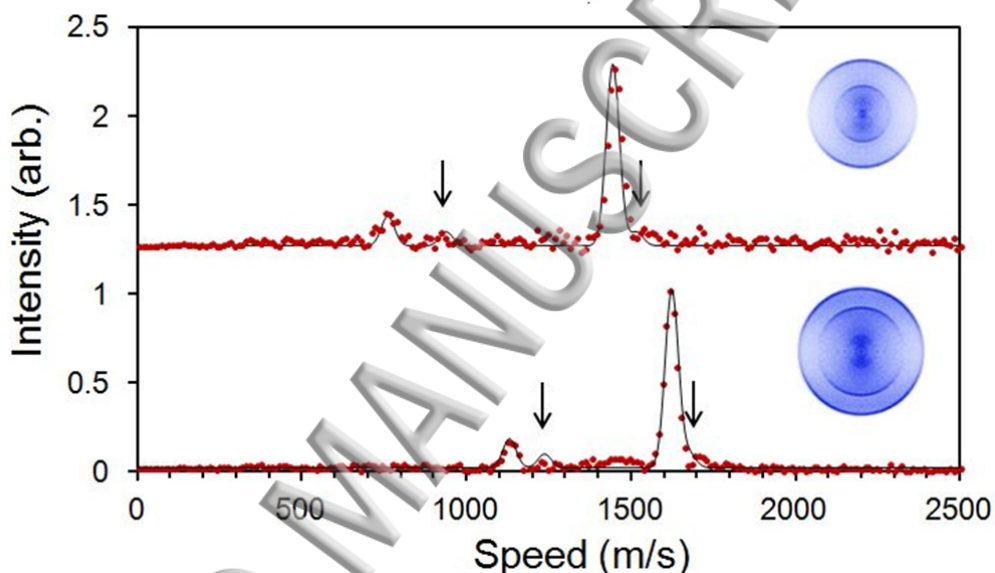


Figure 2. S branch CO ion images with their corresponding speed distributions and simulations at 213.478 nm on the left and 213.615 nm on the right. The inner rings originate from $v=1$ CO while the outer rings originate from $v=0$ CO. The top panel corresponds to $j=63$ for the outer ring and $j=67$ for the inner ring and the bottom panel corresponds to $j=58$ for the outer ring and $j=61$ for the inner ring. Filled circles are for the experimental speed distribution, while the solid lines show the simulated speed distribution. Minor contributions of CO products originating from vibrationally excited parent OCS are also shown and their locations are marked by arrows.

Figure 2 shows two images of one color dissociation at wavelengths corresponding to the overlapping states. Features corresponding to CO ($v=0, j$) (outer ring) and CO ($v=1, j$) (inner ring) products are clearly resolved. The ion images shown have been symmetrized and their corresponding speed distributions (filled circles) from reconstructed images are also shown in

Figure 2. The relative contributions of $v=0$ and $v=1$ to each overlapped peak can be determined by integration of the corresponding features. In addition, the comparison of the speeds associated with the CO $v=0$ and $v=1$ components can be used to provide confirmation of the rotational state assignments. Gaussian peaks were used to simulate the speed distributions in Figure 2, using speeds derived from energy conservation. Based on this analysis we are confident of the final state assignments employed in the spectral simulations. In Figure 2, very weak features are observed near 1550 m/s and 1700 m/s consistent with vibrationally excited OCS parent ($v_2=1$) producing CO ($v=0, j$) fragments. Minor features corresponding to vibrationally excited parent are also present for the $v=1$ CO product channel. The simulated $v=1$ CO product originating from vibrationally excited parent OCS appears at 950 m/s and 1250 m/s for the upper and lower images respectively. Previous studies^{17,19,22,41,42,43} have observed contributions from the photodissociation of vibrationally excited OCS, which are most pronounced at the highest CO rotational states, suggesting that initial parent bending leads to greater final CO rotation. Our observations are consistent with these reports. Based on the intensities of the rotational lines, we find a $v=1$ contribution of approximately 21% which is larger than the theoretical prediction of 13.2%.^{25,44}

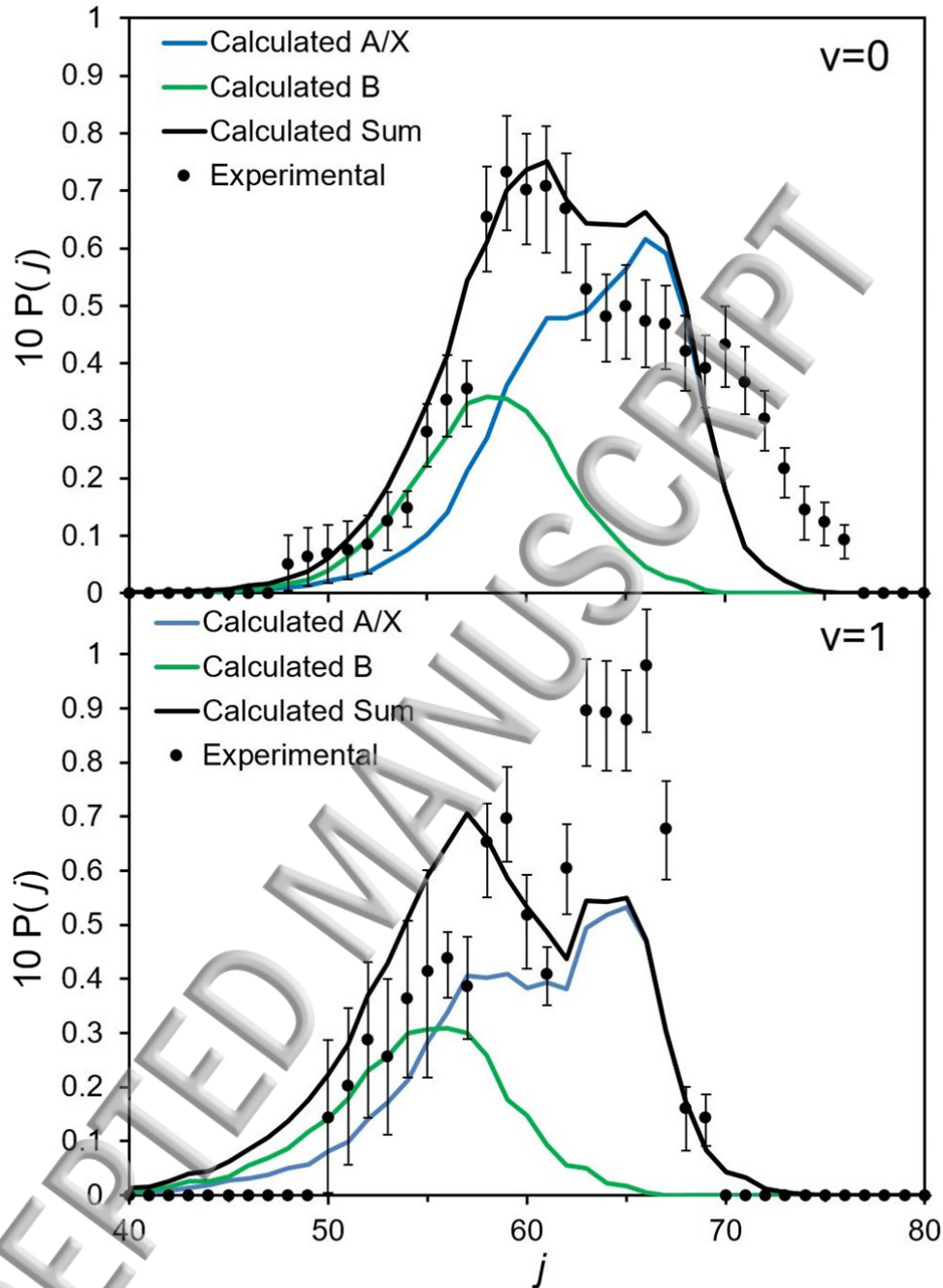


Figure 3. CO Rotational distributions associated with $v=0$ (upper panel) and $v=1$ (lower panel). In both panels, the experimental data are shown with filled circles and compared to the results of classical trajectory calculations (solid lines). The computed contributions from the A/X and B pathways are shown with blue and green lines respectively for both $v=0$ and $v=1$ CO products. The rotational populations have been normalized and scaled.

Figure 3 shows the CO rotational distributions from photodissociation near 214 nm. The experimental population for each CO rovibrational state was obtained from the fitted 2+1 REMPI spectrum shown in Figure 1. The experimental rotational populations have been normalized and are compared to classical trajectory/surface hopping calculations. The computed population contributions to each CO vibrational state from the A/X and B pathways are also shown. The A/X component includes any product that originated in the $2^1A'$ state, while the B pathway is for products from the $1^1A''$ state. Previous studies at longer wavelengths reported a clear bimodal distribution. At wavelengths near 214 nm, however, the two components have almost coalesced, although there are clearly two features present. For $v=0$ products, the lowest rotational state observed is $j=48$. The results from the trajectory calculations match the maximum in the experimental population distribution, although there are some differences at the highest states. The calculations overestimate populations near $j=65$ and underestimate those for $j>70$. The experimental CO $v=1$ rotational distribution is qualitatively in agreement with calculated results and the shift of the distributions to lower j is well reproduced. The rotational population starts at higher j and ends at lower j than the $v=0$ rotational distribution.

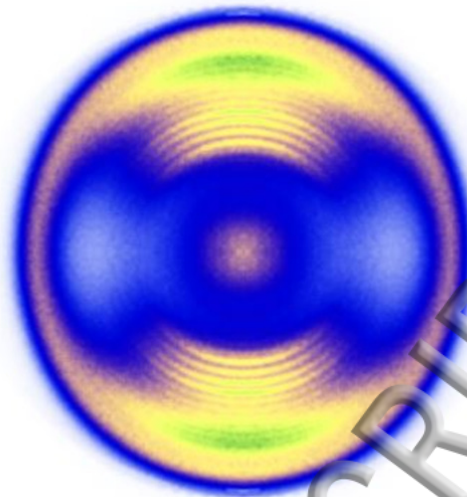


Figure 4. A DC sliced S(1D_2) ion image arising from OCS photodissociation at 214.2 nm with a VH geometry.

In order to confirm the rotational distribution derived from the CO REMPI, we collected ion images of the S(1D_2) fragment. Both DC sliced and crushed images were obtained and analyzed. Figure 4 shows a typical DC sliced S(1D_2) image arising from OCS photodissociation at 214.2 nm with a vertically polarized pump laser beam and a horizontally polarized probe laser beam. The clear ring-pattern structure in the image corresponds to specific rotational states of the coincident CO fragment due to energy conservation, given by

$$E_{\text{avail}} = h\nu - D_{00} + E_{\text{int}}(\text{OCS}) = E_{\text{int}}(\text{CO}) + E_{\text{int}}(\text{S}) + E_{\text{trans}} \quad (5)$$

where E_{avail} is the available energy of photochemical products; $h\nu$ is the dissociation photon energy; D_{00} is the dissociation energy of OCS; $E_{\text{int}}(\text{OCS})$, $E_{\text{int}}(\text{CO})$, $E_{\text{int}}(\text{S})$ are internal energy of OCS, CO, and S respectively; and E_{trans} is the translational energy of two fragments. We employed a value of D_{00} of 34641 cm^{-1} based on the work of Komissarov *et al.*³² The S(1D_2) speed distribution derived from Figure 4 is shown in Figure 5.

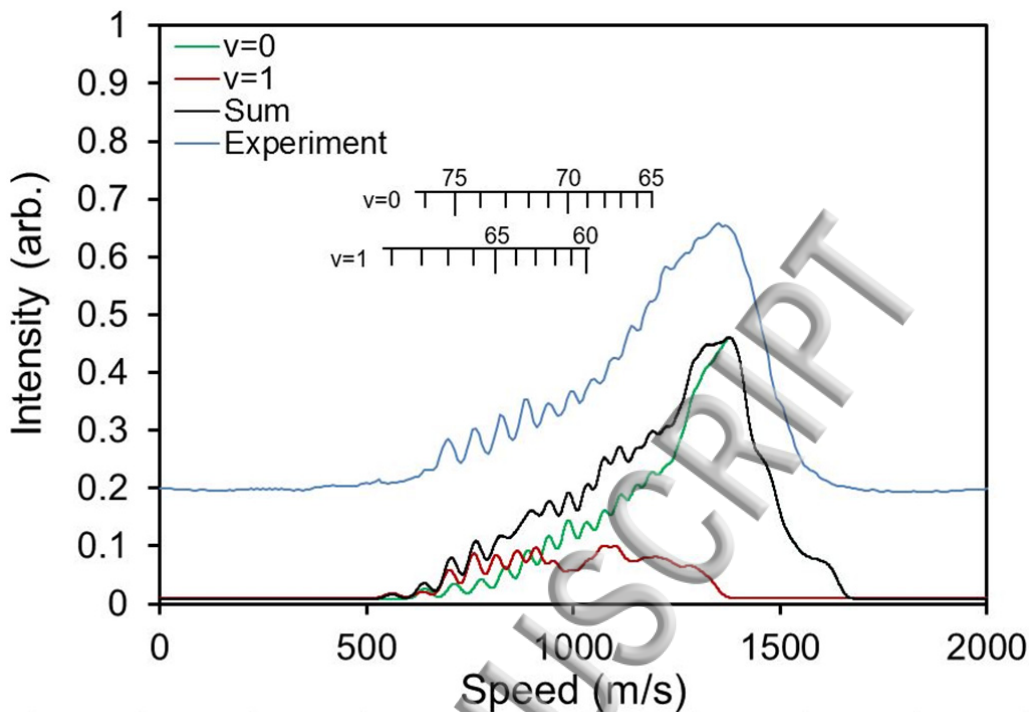


Figure 5. The speed distribution derived from the DC sliced $S(1D_2)$ image shown in Figure 4. The simulation consists of two components based on the rotational distributions from the REMPI spectrum, $v=0$ in green and $v=1$ in red. The $v=1$ population of 21% is shown which was obtained from the REMPI spectrum.

The CO vibrational distribution can also be extracted from the sulfur images. Forward convolution simulations (solid black) using the optimized CO rotational state distributions for both the $v=0$ (green) and the $v=1$ (red) components derived from the CO REMPI spectra are shown in Figure 5. The ratio between the $v=0$ and $v=1$ states was adjusted in order to find the best fit to the sulfur speed distribution. The best fit, shown in Figure 5, resulted in a $v=1$ contribution of $21 \pm 8\%$, in excellent agreement with the result obtained from the REMPI spectrum.

The trajectory calculations predict that the $v=1$ population should be small but increase as the wavelength becomes shorter. The calculated populations in $v=1$ from McBane *et al.* are 2.3%, 2.7%, 4.7, 13.5%, and 13.2% at 248, 235, 230, 222, and 214.5 nm respectively.^{25,44} The calculations therefore underestimate the 214.5 nm vibrational population modestly.

The 21% $v=1$ population found here is more surprising because of its discordance with experimental results at other wavelengths. Several groups^{14,15} have detected CO following 230 nm dissociation using 2+1 REMPI through the B state; it is not too surprising that most of those experiments did not observe highly rotationally excited CO, since the B state is predissociated in $v=1$ above $j=17$, and more strongly predissociated above $j=37$.⁴⁵ Rijs *et al.*, using the same technique with photoelectron detection, did see a very weak spectrum corresponding to the Q branch of the (1-1) band.¹⁵ The absence of rotational resolution in that spectrum, while the spectroscopically similar (0-0) band nearby was fully resolved, further indicates that predissociation at high j limits the sensitivity of the B-X REMPI probe. The 217 nm experiment of Sato *et al.* used CO REMPI through the C state on a Q branch.¹⁴ In that spectrum the (1-1) band can be expected to be hidden under the (0-0) band, except for the $j<50$ tail of the $v=1$ rotational distribution. In fact there is a small tail extending to lower j in their published spectrum (Fig. 7) between 217.45 and 217.5 nm that may well be the (1-1) band. However, the 222 nm experiment of Sivakumar *et al.*, using one-photon laser induced fluorescence through the A state, should have been sensitive to $v=1$ CO, and that group found no $v=1$ during “extensive searches”.¹³

Several other groups^{17,18,22,43,46} have depended on REMPI of the sulfur atom, and extracted CO internal state distributions from the sulfur speed distributions. In those

experiments it is hard to identify $v=1$ unless the sulfur speed distribution is fully rotationally resolved, as is evident in Figure 5; the slower atoms correlated with $v=1$ tend to merge with similarly slow atoms coincident with higher rotational levels in $v=0$.

In our experiment, predissociation or dissociative ionization of the E state during REMPI detection are also possibilities; these effects have been reported at $j \leq 31$.^{27,38,47} The C^+ yield from CO^+ is j -state dependent and is not negligible near $j=20$. However, the influence of predissociation or dissociative ionization at $j > 50$ has not been reported. Attempts were made to search for C^+ but no signal was detected, so we conclude that the yield of C^+ is unlikely to be significant. The $v=1$ level in the E state is more likely than $v=0$ to suffer these effects so they would probably cause an underestimate, rather than an overestimate, of the $v=1$ population.

We conclude that the branching ratio into $v=1$ changes substantially between 222 and 214 nm. Our trajectory calculations, and the quantum calculations reported in reference 25, do suggest a fairly steep rise (a factor of about 3) in the $v=1$ population between 230 and 222 nm. One possibility is that the steep rise does occur, but at somewhat shorter wavelengths, so that the small $v=1$ population at 222 nm was below the detection limit of the LIF experiment but the $v=1$ yield rises to more than 14% by 214 nm. Evidence against that speculation is that in preliminary two-color experiments we have detected substantial $v=1$ product from 230 nm photolysis using the 214 nm E-state probe technique. Given the surprising inconsistencies among the different observations we must regard the wavelength dependence of the product vibrational distribution as open for investigation. Our experiments definitely indicate that 214 nm dissociation produces a nonnegligible amount of $v=1$ CO.

B. Computed Rotational Distributions and Interpretation

When the rotational distribution is compared to those at longer wavelengths, a consistent trend appears: with decreasing photolysis wavelength the two channels merge together, the high j component increases in intensity, and the rotational distribution moves to higher j . Our rotational distribution shows a higher contribution from the $2^1A'$ channel than Sato *et al.* found at 217 nm.¹⁴ The higher j product channel (from pure $2^1A'$ state) at 217 nm is still relatively low in intensity compared to the lower j channel (from a mixed contribution of both $2^1A'$ and $1^1A'$ states). In the present work at 214 nm the higher j component shows comparable intensity to lower j components. Dissociation at 217 nm yields a rotational distribution that peaks at $j=58$ and $j=65$, while this work shows peaks at $j=60$ and 70 . Trajectory calculations suggest that both of these differences are due to the shape of excited state potential energy surface. The rotationally excited products are the result of simultaneous bond breaking and bending. The molecule starts on the excited state surface in a nearly linear configuration, with γ of just a few degrees, while the A and B states have minima near $\gamma=48^\circ$ and 38° respectively. During the dissociation the bending potential applies a torque that increases γ (and its time derivative $\dot{\gamma}$) until the minimum is reached; after that, the potential serves to slow the rotation. The differences in dissociation wavelength result in different starting points for the trajectories on the excited state surface, which eventually result in different deceleration forces on the OCS bending. As the wavelength of excitation decreases, excited state molecules start in regions with higher bending forces and the deceleration effect becomes less pronounced, resulting in products with more rotational excitation. The non-adiabatic crossing from the $2^1A'$ (A state) to the $1^1A'$ (X state) takes place just after the bending of OCS reaches the “deceleration region”,

so that molecules making that transition retain the high rotational angular momentum they acquired in the initial stages of the dissociation.

The left panels in Figure 6 show “phase space plots”, $j(t)$ vs. $\gamma(t)$, for 15 randomly selected trajectories beginning on the A state at 230 and 214 nm. The first hop from A to X is marked with a dot; segments of each trajectory on the X state are plotted in red. The surface hops fall into “early” and “late” groups because of the coordinate dependence of the nonadiabatic coupling.¹¹ At both wavelengths, trajectories that make early hops and remain on the X state are decelerated less than those that complete most of the trajectory on the A state. The early-hop groups therefore finish with higher j on average. At 230 nm, the early-hop trajectories are clearly segregated from the others that hop late or not at all, while at 214 nm the separation is not as clear because the A-state-only trajectories are not as strongly affected by the angular decelerating force. The right panels give the rotational distributions from the complete trajectory sets, separated into sets that do make an early hop and those that do not. The merging of the pure-A and the nonadiabatic A-X components of the rotational distribution with decreasing wavelength is clear. Some trajectories make an early hop to X but hop quickly back to A; those still feel the decelerating force and are the source of the “tail” that extends to lower j in the early-hop rotational distribution.

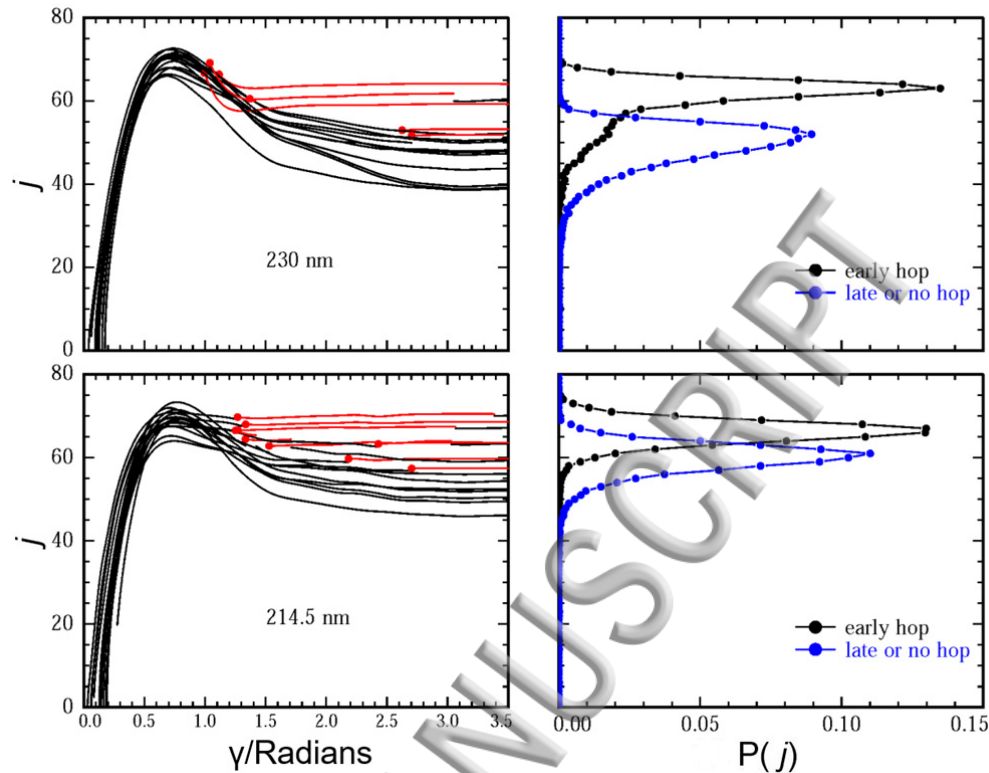


Figure 6. Left panels: Individual trajectories begun on the A state and propagated with the possibility of surface hopping to X, plotted in (γ, j) coordinates. Portions of each trajectory on the A state are in black and on the X state are in red, with the first hop from A to X indicated with a red dot. Right panels: rotational distributions from the entire trajectory set (50,000 trajectories at each wavelength), divided into two groups that did or did not hop from A to X while $\gamma < 1.7$.

C. Vector Correlations and Contributions of $2^1A'$ and $1^1A''$ States

We collected a series of CO images to determine the j -dependent relative contribution from the $2^1A'$ and $1^1A''$ states. Figure 7 shows three CO images acquired using R-branch transitions that display distinct anisotropy. On the leftmost image, the outer ring corresponds to $j=57, v=0$ and shows weak four-fold symmetry, with extra intensity at the 90 degree image angle. In contrast, the image from $j=71, v=0$ shows more pronounced four-fold symmetry, with very low signal intensities at 90 degrees. The image from $j=62, v=0$ shows intermediate

anisotropy. Image anisotropies result from linear laser polarization and fragment vector correlations. The linear polarization provides lab frame alignment with the transition dipole moment and preferential detection of rotational angular momentum vectors. Changes in the image anisotropies from low j to high j CO images quantitatively reveal changes in vector correlation.

Several different formalisms have been used to describe vector correlations. Dixon's semiclassical bipolar moment formalism offers a description with straightforward physical interpretations.⁴⁸ Conveniently, the $\beta_0^2(20)$ (μ - \mathbf{v}), $\beta_0^0(22)$ (\mathbf{v} - \mathbf{j}), and $\beta_0^2(02)$ (μ - \mathbf{j}) low order bipolar moments can be interpreted semiclassically as the expectation values of the 2nd Legendre polynomial: $\langle P_2(\cos\theta) \rangle$ where θ is the angle between two relevant vectors. For example, $\beta_0^2(02)$, where θ is the angle between the μ and \mathbf{j} vectors, gives limiting values ranging from -0.5 if the vectors are perpendicular ($2^1A'$ state in OCS), to 1 if the vectors are parallel ($1^1A''$ state in OCS). j dependent bipolar moments can be derived from CO image anisotropies.

Angular distributions were extracted from each image by integrating the intensity over a narrow radial range (5-8 pixels) around the outer edge of each crushed image. When the measured images consist of a single speed component, the signal at the maximum ion cloud radius is equivalent to the angular distribution that would be obtained from sliced imaging.⁴⁹

The angular distributions of ion images can be expressed as weighted sums of Legendre polynomials,

$$I^{FG}(\theta) = 1 + \beta_2^{FG} P_2(\cos \theta) + \beta_4^{FG} P_4(\cos \theta) + \beta_6^{FG} P_6(\cos \theta) \quad (6)$$

where the β_k^{FG} are called image anisotropy parameters; F and G stand for the lab frame pump and probe polarizations respectively, which in these experiments are both polarized along a vector X parallel to the imaging plane. The X axis defines the origin of the imaging angle θ . Up to 6th order polynomials are applied; in the semi-classical limit, orders higher than six may be neglected for a two photon process.⁵⁰ In the high- j semiclassical limit, the contribution of coherence effects to the angular momentum polarization of CO is $1/j$ dependent, so the high- j limit is appropriate for CO fragments with $j > 50$ where these effects are negligible.

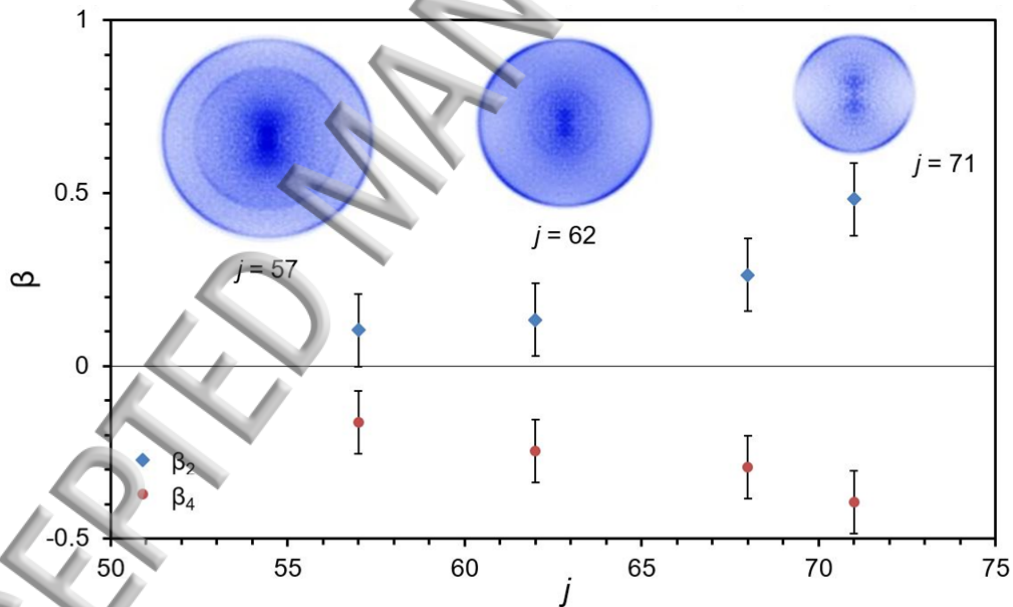


Figure 7. R branch CO ($v=0$) images from different rotational states. The insets show the corresponding image anisotropy parameters. From left to right images are taken at 214.291 nm, 214.18 nm, and 214.027 nm.

Bipolar moments can be calculated from measured image anisotropy parameters.^{49,51} We have recently extended the methodology of Grubb *et al.* (applicable to 1+1 REMPI detection)

to 2+1 REMPI detection. This method follows the same general approach as the work of Grubb *et al.*:

$$\beta_k^{FG} = \int_0^\pi I[\theta, \Phi, \theta_\varepsilon, \beta_Q^K(k_1, k_2)] P_k(\cos \theta) \frac{2k+1}{2} \sin \theta d\theta, \quad (7)$$

where θ is the angle between recoil velocity vector of the photofragment \mathbf{v} and probe laser polarization vector \mathbf{P} , θ_ε is the angle between \mathbf{v} and dissociation laser polarization vector \mathbf{E} , Φ is the azimuthal angle between \mathbf{P} and \mathbf{E} about \mathbf{v} , θ is the lab frame image angle, and the $\beta_Q^K(k_1, k_2)$ are a set of Dixon's bipolar moments. In the case of DC-sliced images with vertically polarized dissociation and probe lasers, the θ_ε and θ angles both become image angle θ , while Φ becomes 0.⁴⁹ $I[\theta, \Phi, \theta_\varepsilon, \beta_Q^K(k_1, k_2)]$ is a function describing the photofragment detection probability in the molecular frame.^{52,53} We have extended equation 16 from reference 52 to include $k=4$ terms which emerge from 2+1 detection. By using the bridging equations 7(a-e) from Rakitzis *et al.* and equations 2-5 from Denzer *et al.* we replace Rakitzis's molecular frame polarization parameter, $a_q^{(k)}(p)$, in the photofragment detection probability function with bipolar moments.^{54,55} In this way, we obtain image anisotropies as functions of bipolar moments and detection laser geometries. The function $I[\theta, \Phi, \theta_\varepsilon, \beta_Q^K(k_1, k_2)]$ in equation 7 contains detection sensitivity factor, s_k , based on Table 1 from published work by Rakitzis and Alexander.⁵³ (These were called alignment sensitivity coefficient in Grubb's work) At high j , the O/S branch s_2 and s_4 factors included in I approach the limiting values of $-5/7$ and $3/7$ respectively, while the P/R branch s_2 and s_4 factors approach $5/14$ and $-12/7$ respectively.

For 1 photon dissociation followed by 2+1 REMPI detection, there are 9 applicable bipolar moments: $\beta_0^2(20)$, $\beta_0^2(02)$, $\beta_0^2(22)$, $\beta_0^0(22)$, $\beta_0^2(24)$, $\beta_0^2(42)$, $\beta_0^2(44)$, $\beta_0^0(44)$, $\beta_0^2(64)$. In the semi-classical limit the moments $\beta_0^2(42)$ and $\beta_0^2(64)$ can be expressed as linear combinations of other bipolar moments. Using equation 4 from reference 54 and equation 7d from reference 55, and assuming the interference term is negligible, we find

$$\beta_0^2(42) = \frac{7}{12}\beta_0^2(02) - \frac{5}{12}\beta_0^2(22) \quad (8)$$

$$\beta_0^2(64) = \frac{11}{14}\beta_0^2(24) - \frac{3}{14}\beta_0^2(44). \quad (9)$$

We also constrained the value of $\beta_0^0(22)$ and $\beta_0^0(44)$ to -0.5 and 0.375, respectively, to reflect the perpendicular \mathbf{v} and \mathbf{j} vectors expected for dissociation from jet-cooled parent OCS. Five image anisotropy parameters are needed to extract the remaining five independent bipolar moments. In the work of Grubb *et al.* the analysis involved β_k^{FG} from three detection geometries, VV, VH and HV. In many cases however, for rapid dissociation via a parallel transition, high quality HV geometry sliced images are hard to obtain. In such cases, VV images from an S and an R branch (or an O and a P branch) are more accessible. We find that full sets of β_2^{xx} , β_4^{xx} , β_6^{xx} coefficients of an S branch and an R branch image of the same j state, using one color vertical polarization, can provide sufficient information for extracting the relevant bipolar moments. More details of the new mathematical relations will be discussed elsewhere.⁵⁶

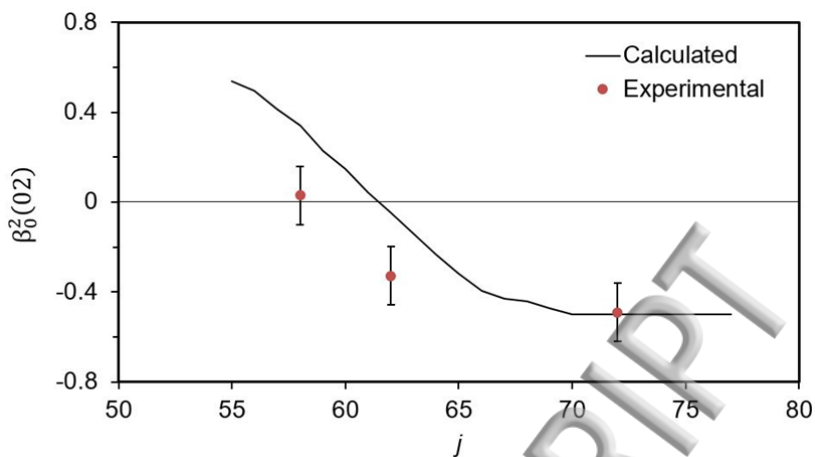


Figure 8. The $\beta_0^2(02)$ bipolar moment for different rotational states. The experimental values are represented by the filled circles at $j=58, 62,$ and 72 . The calculation is represented by the black line.

We have extracted full sets of bipolar moments from S and R branch image pairs at $j=58, 62$ and 71 ($v=0$) to study the j -dependence of the vector correlations, particularly the alignment (μ - ν) bipolar moment $\beta_0^2(02)$. The results are shown in Figure 8 along with the calculated prediction that reflects fractional contributions of A' and A'' absorption to each final state. We find values close to the negative limiting case of $\beta_0^2(02)$ at high j which is consistent with pure $2^1A'$ state (μ perpendicular to j). At low j $\beta_0^2(02)$ is close to 0, reflecting a mixture of the $2^1A'$ and $1^1A''$ channels. A value of $\beta_0^2(02)$ near 0 indicates that the $2^1A'$ state contribution is greater than 50% since an equal contribution of the $2^1A'$ and $1^1A''$ states should yield a value of 0.25 for $\beta_0^2(02)$. The calculations predict the trend in $\beta_0^2(02)$ values accurately, but give too large an A'' contribution at lower j . The error could come either from inaccuracy in the computed transition moments or in the rotational distributions predicted for the A and B states. Both problems may be present but the second is likely to be the main cause of the discrepancy. The potential energy surfaces used were empirically modified to give good rotational

distributions at 235 nm, and we may expect errors in their predictions that grow as the dissociation wavelength moves farther from that “anchor” point.

j -dependent image anisotropy parameters were also derived from a crushed $S(^1D_2)$ image. Due to orbital alignment of the S atom, the β^{VV}_2 parameter is not a direct indicator of the μ - v correlation.^{20,21,43,46} However, the β^{VV}_2 values derived from the $S(^1D_2)$ image show a general trend from near 0 at low j to near 1 at high j which is consistent with our derived $\beta_0^2(20)$ values from the CO images.

The inner ring of the CO image on the left in Figure 7 corresponds to $v=1$, $j=60$ CO products. This inner ring shows more significant four-fold symmetry than the outer ring (lower j). Anisotropic inner rings are observed in several other CO S branch and R branch images. Although no detailed analysis to determine vector correlations was performed on $v=1$ images, $v=0$ and $v=1$ CO images show the same j -dependent anisotropy trend. We therefore expect that the $v=0$ and $v=1$ products have similar vector correlations. Computations of rotational contributions of $2^1A'$ (A state) and $1^1A''$ (B state) to the $v=1$ rotational distribution were also conducted and the results are qualitatively consistent with the trend shown on these images.

Although the measured bipolar moments can be affected by depolarization due to initial parent rotation, no attempt was made to correct the values to account for depolarization. We anticipate that following supersonic expansion, the OCS parent has low rotational temperature.

Table II. Bipolar moments obtained from CO images.

j	58	62	72
$\beta_0^2(02)$	0.03±0.13	-0.33±0.13	-0.49±0.13
$\beta_0^2(20)$	0.14±0.07	0.26±0.07	0.32±0.07

V. Conclusion

In this paper, both velocity map ion imaging experiments and computational results are presented for OCS photodissociation in the 214 nm region. Product distributions were measured by probing both CO and S(1D_2) fragments. One color laser photodissociation and 2+1 REMPI probing the E-X transition were conducted to obtain a rotational distribution of CO products for both $v=0$ and $v=1$. Two color S(1D_2) images show a rovibrational product distribution consistent with the one from the CO REMPI. The rotational distributions for both $v=0$ and $v=1$ CO show two components that are shifted toward higher j compared to longer dissociation wavelengths and nearly coalesced. The dissociation dynamics are similar to those at longer wavelengths, except that a higher fraction of vibrationally excited CO appears. The lower j component is produced through incoherent excitation to $2^1A'$ and $1^1A''$ followed by direct dissociation on those surfaces. The high j component is a result of non-adiabatic crossing from the $2^1A'$ state to the ground state and consequent avoidance of rotational deceleration from the inner wall of the bending potential of A-state OCS. The $v=1$ CO rotational distribution generally has the same shape, but is shifted to lower j by 2-3 quanta.

Vector correlation information in the form of bipolar moments was extracted from signal images using a new procedure suitable for 2+1 REMPI measurements in a single polarization geometry on multiple spectral branches. The resulting moments, in particular the rotational alignment of product CO, are consistent with the earlier observations of Sivakumar *et al.* at 222 nm and indicate a substantial contribution of $1^1A''$ absorption to the lower- j part of the rotational distribution.¹³

Acknowledgements

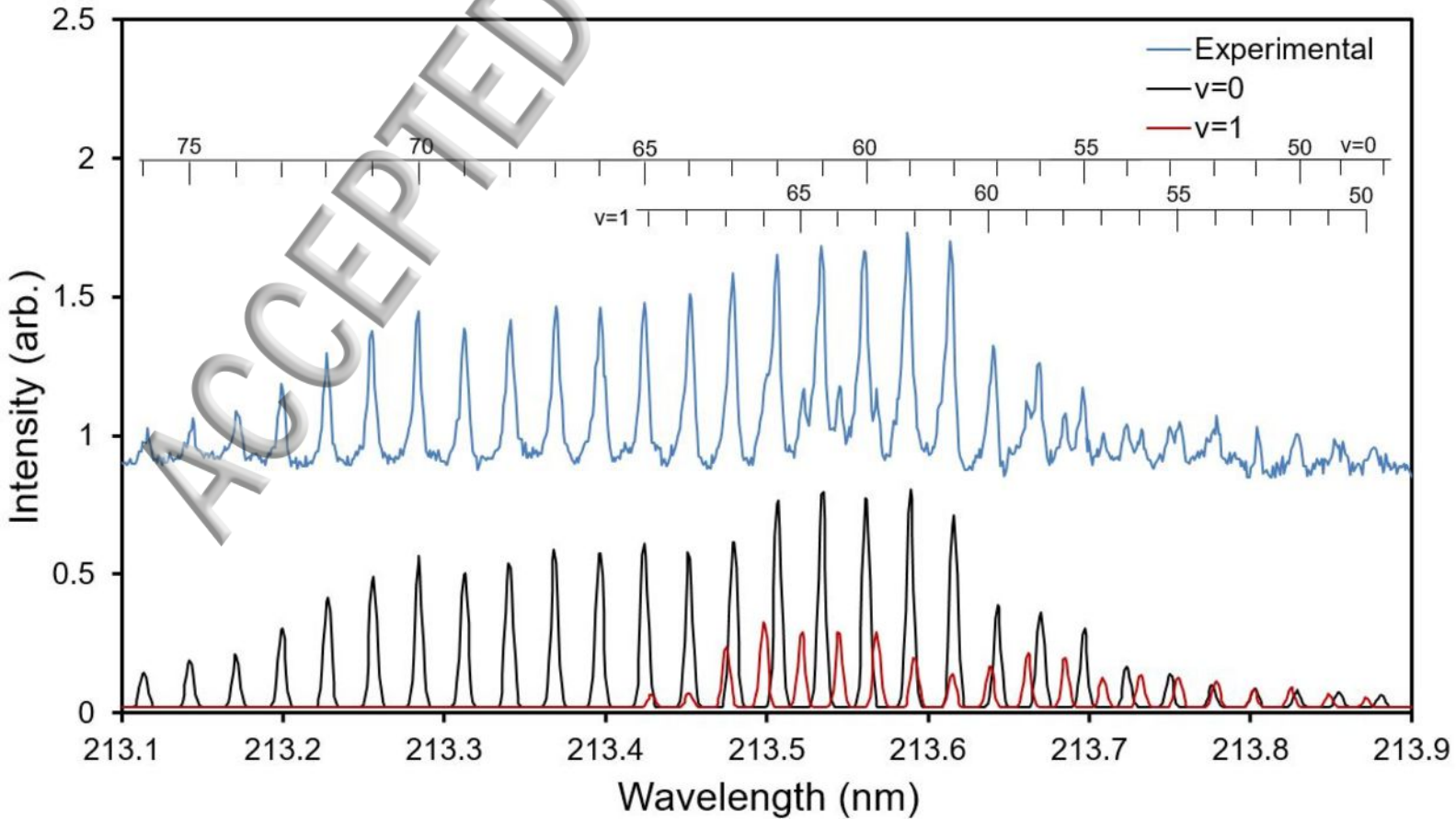
The authors would like to thank Gregory Hall, Peter Rakitzis and Michael Grubb for helpful discussions. We would like to thank Paul Houston for providing much of the instrumentation used in this study. We would also like to thank Will Seward, Ron Page and Timothy Pehl for technical assistance. Support for this project was provided by the Robert A. Welch Foundation (A-1405).

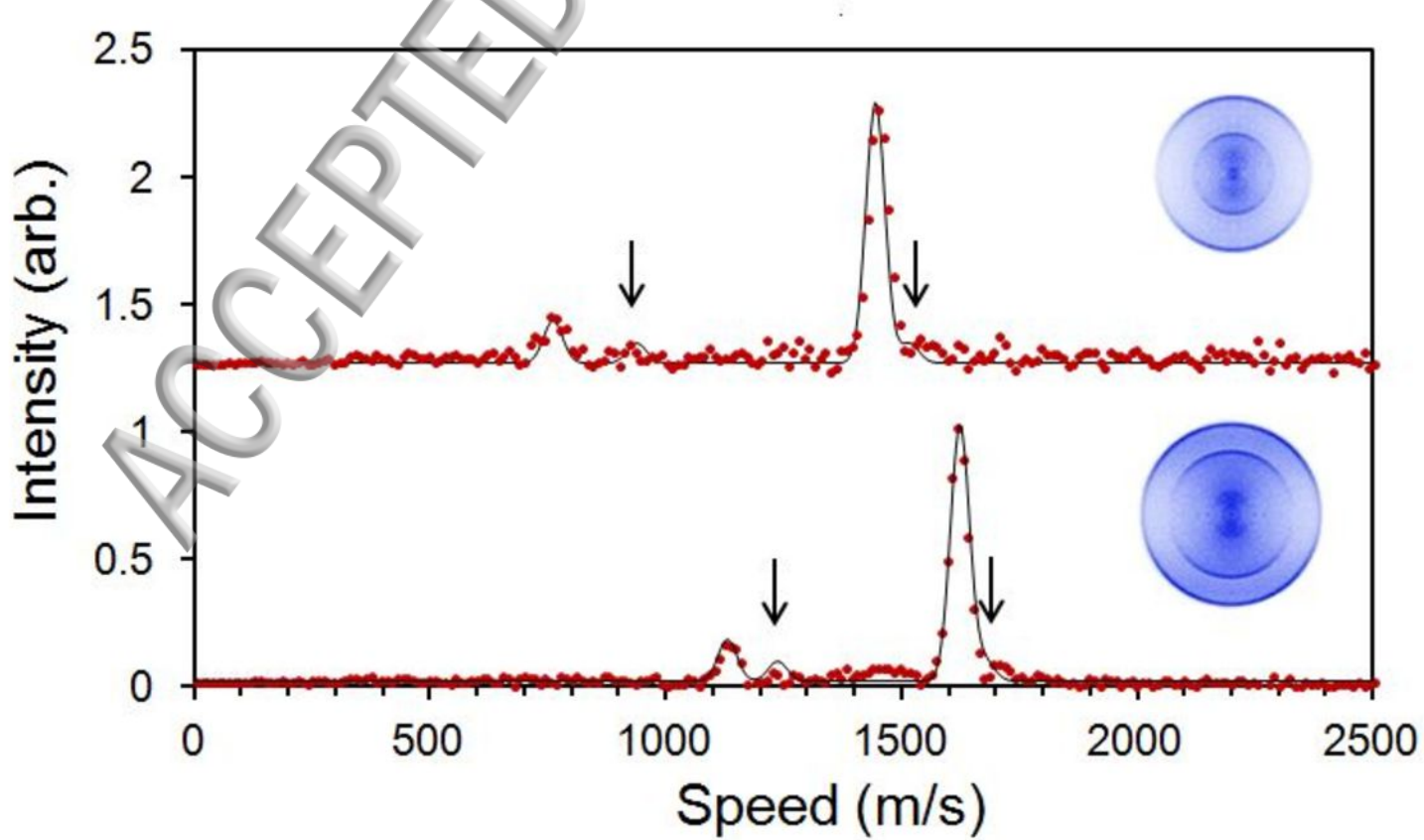
References

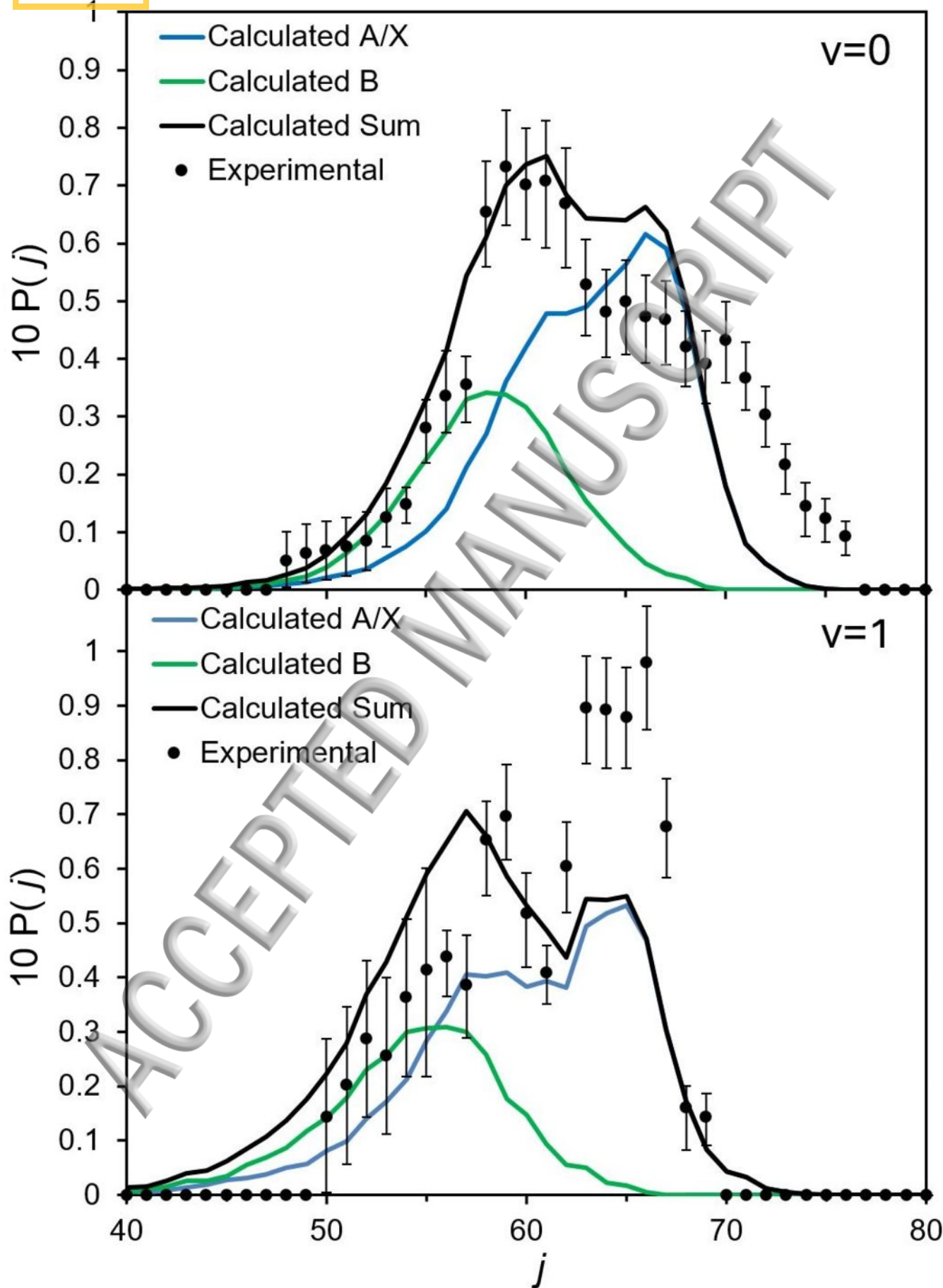
- ¹ P. J. Crutzen, *Geophys. Res. Lett.* **3**, 73 (1976).
- ² J. Notholt, Z. Kuang, C. P. Rinsland, G. C. Toon, M. Rex, N. Jones, T. Albrecht, H. Deckelmann, J. Krieg, C. Weinzierl, H. Bingemer, R. Weller, O. Schrems, *Science* **300**, 307 (2003).
- ³ M. Chin and D. D. Davis, *J. Geophys. Res-Atmos.* **100**, 8993 (1995).
- ⁴ M. O. Andreae and P. J. Crutzen, *Science* **276**, 1052 (1997).
- ⁵ G. Krysztofiak, Y. V. Te, V. Catoire, G. Berthet, G. C. Toon, F. Jegou, P. Jeseck, C. Robert, *Atmos. Ocean.* **53**, 89 (2015).
- ⁶ S. Hattori, S. O. Danielache, M. S. Johnson, J. A. Schmidt, H. G. Kjaergaard, S. Toyoda, Y. Ueno, N. Yoshida, *Atmos. Chem. Phys.* **11**, 10293 (2011).
- ⁷ L. T. Molina, J. J. Lamb, M. J. Molina, *Geophys. Res. Lett.* **8**, 1008 (1981).
- ⁸ C. Y. R. Wu, F. Z. Chen, D. L. Judge, *J. Quant. Spectrosc. Ra.* **61**, 265 (1999).

- ⁹ S. O. Danielache, S. Nanbu, C. Eskebjerg, M. S. Johnson, N. Yoshida, J. Chem. Phys. **131**, 024307 (2009).
- ¹⁰ K. Sunanda, B. N. Rajasekhar, P. Saraswathy, B. N. Jagatap, J. Quant. Spectrosc. Ra. **113**, 58 (2012).
- ¹¹ J. A. Schmidt, M. S. Johnson, G. C. McBane, R. Schinke, J. Chem. Phys. **137**, 054313 (2012).
- ¹² G. Nan, I. Burak, P. L. Houston, Chem. Phys. Lett. **209** 383 (1993).
- ¹³ N. Sivakumar, G. E. Hall, P. L. Houston, J. W. Hepburn, I. Burak, J. Chem. Phys. **88**, 3692 (1988).
- ¹⁴ Y. Sato, Y. Matsumi, M. Kawasaki, K. Tsukiyama, R. Bersohn, J. Phys. Chem. **99**, 16307 (1995).
- ¹⁵ A. M. Rjis, E. H. G. Backus, C. A. de Lange, M. H. M. Janssen, N. P. C. Westwood, K. Wang, V. McKoy, J. Chem. Phys. **116**, 2776, (2002).
- ¹⁶ S. K. Lee, R. Silva, S. Thamanna, O. S. Vasyutinskii, A. G. Suits, J. Chem. Phys. **125**, 144318 (2006).
- ¹⁷ A. J. van den Brom, T. P. Rakitzis, J. van Heyst, T. N. Kitsopoulos, S. R. Jezowski, M. H. M. Janssen, Chem. Phys. **117**, 4255 (2002)
- ¹⁸ T. Suzuki, H. Katayanagi, S. Nanbu, M. Aoyagi, J. Chem. Phys. **109**, 5778 (1998).
- ¹⁹ M. H. Kim, W. Li, S. K. Lee, A. G. Suits, Can. J. Chem. **82**, 880 (2004).
- ²⁰ Y. Mo, H. Katayanagi, M. C. Heaven, T. Suzuki, Phys. Rev. Lett. **77**, 830 (1996)
- ²¹ T. P. Rakitzis, P. C. Samartzis, T. N. Kitsopoulos, Phys. Rev. Lett. **87**, 123001 (2001)
- ²² A. J. van den Brom, T. P. Rakitzis, M. H. M. Janssen, J. Chem. Phys. **121**, 11645 (2004).
- ²³ R. N. Zare, Ph.D. thesis, Harvard University, Cambridge, MA, 1964.
- ²⁴ R. N. Zare and D. R. Herschbach, Proc. IEEE **51**, 173 (1963).
- ²⁵ G. C. McBane, J. A. Schmidt, M. S. Johnson, R. Schinke, J. Chem. Phys. **138**, 094314 (2013).
- ²⁶ O. Tokal, Ph.D. thesis, Cornell University, 2011.
- ²⁷ M. Hines, Ph.D. thesis, Stanford University, 1992.
- ²⁸ Y. Pak, R. C. Woods, J. Chem. Phys. **107**, 5094 (1997).
- ²⁹ G. Black and L. E. Jusinski, J. Chem. Phys. **82**, 789 (1985).
- ³⁰ J. Steadman and T. Baer, J. Chem. Phys. **89**, 5507 (1988).
- ³¹ G. M. Roberts, J. L. Nixon, J. Lecointre, E. Wrede, J. R. R. Verlet, Rev. Sci. Instrum. **80**, 053104 (2009).
- ³² A. V. Komissarov, M. P. Minitti, A. G. Suits, G. E. Hall, J. Chem. Phys. **124**, 014303 (2006).
- ³³ G. C. McBane and R. Schinke, J. Chem. Phys. **136**, 044314 (2012).
- ³⁴ J. A. Schmidt and J. M. H. Olsen, J. Chem. Phys. **141**, 184310 (2014).
- ³⁵ J. A. Schmidt, private communication
- ³⁶ J. C. Tully, J. Chem. Phys. **93**, 1061 (1990).
- ³⁷ R. Schinke and G. C. McBane, J. Chem. Phys. **132**, 044305 (2010).
- ³⁸ J. Baker, J. L. Lemaire, S. Couris, A. Vient, D. Malmasson, F. A. Rostas, Chem. Phys. **178**, 569 (1993).

- ³⁹ E. K. Plyler, L. R. Blaine, W. S. Connor, J. Opt. Soc. Am. **45**, 102 (1955).
- ⁴⁰ G. Lucchese, R. R. Lucchese, S. W. North, J. Chem. Educ. **87**, 345 (2010).
- ⁴¹ A. Sugita, M. Mashino, M. Kawasaki, Y. Matsumi, R. Bersohn, G. Trott-Kriegeskorte, and K.-H. Gericke. J. Chem. Phys. **112**, 7095 (2000)
- ⁴² H. Katayanagi and T. Suzuki. Chem. Phys. Lett. **360**, 104 (2002)
- ⁴³ L. M. Lipciuc, T. P. Rakitzis, L. W. Meerts, G. C. Groenenboom, M. H. M. Janssen, Phys. Chem. Chem. Phys. **13**, 8549 (2011).
- ⁴⁴ The values reported here are from trajectories including surface hopping, while those reported in Ref. [25] are from quantum calculations without coupling to the ground state.
- ⁴⁵ M. Eidelsberg, J. Y. Roncin, A. Le Floch, F. Launay, C. Letzelter, J. Rostas. J. Mol. Spectrosc. **121**, 309 (1987).
- ⁴⁶ M. Brouard, A. V. Green, F. Quadrini, C. Vallance, J. Chem. Phys. **127**, 084304 (2007).
- ⁴⁷ M.A. Hines, H. A. Michelsen, R. N. Zare J. Chem. Phys. **93**, 8557 (1990)
- ⁴⁸ R. N. Dixon, J. Chem. Phys. **85**, 1866 (1986).
- ⁴⁹ M. P. Grubb, M. L. Warter, C. D. Freeman, N. A. West, K. M. Usakoski, K. M. Johnson, J. A. Bartz, S. W. North, J. Chem. Phys. **135**, 094201 (2011).
- M. P. Grubb, M. L. Warter, C. D. Freeman, N. A. West, K. M. Usakoski, K. M. Johnson, J. A. Bartz, S. W. North, Erratum: [J. Chem. Phys. **135**, 094201 (2011)] J. Chem. Phys. **136**, 219901 (2012).
- ⁵⁰ M. Docker, Chem. Phys. **135**, 405 (1989).
- ⁵¹ M. P. Grubb, M. L. Warter, S. W. North, Phys. Chem. Chem. Phys. **14**, 6733 (2012).
- ⁵² T. P. Rakitzis and R. N. Zare, J. Chem. Phys. **110**, 3341 (1999).
- ⁵³ T. P. Rakitzis and A. J. Alexander, J. Chem. Phys. **132**, 224310 (2010).
- ⁵⁴ T. P. Rakitzis, G. E. Hall, M. L. Costen, R. N. Zare, J. Chem. Phys. **111**, 8751 (1999).
- ⁵⁵ S. W. Denzer, S. J. Horrocks, P. J. Pearson, G. A. D. Ritchie, Phys. Chem. Chem. Phys. **8**, 1954 (2006).
- ⁵⁶ A paper about our method of extracting vector correlations from 2+1 REMPI Sliced ion images is in preparation







ACCEPTED MANUSCRIPT

